ORIGINAL PAPER

Electrochemical performance of Mg-air batteries based on AZ series magnesium alloys

Jingling Ma[1,2] · Guangxin Wang[1] · Yaqiong Li[1] · Fengzhang Ren[2] · Alex A. Volinsky[3]

Abstract

The purpose of this study is to select a common commercial Mg alloy to function as an anode for Mg-air batteries, with low anode passivation and minimal hydrogen evolution-induced corrosion being desirable characteristics. Corrosion and discharge performance of 3N5 Mg, AZ31, AZ61, and AZ91 alloys was studied. Corrosion susceptibility decreases and anode utilization factor gradually increases with Al content for the 3N5 Mg, AZ31, and AZ61 alloys. The key factors for these results are associated with the $Mg_{17}Al_{12}$ phase, which can act as a barrier to prevent the self-peeling of discharge products. For the AZ91 alloy, the addition of about 9 wt% Al drastically increases discharge activation. Electrochemical impedance spectroscopy and scanning electron microscopy support the results of electrochemical and discharge performance tests. Therefore, AZ61 alloy is the best-suited anode material for the Mg-air batteries in the 0.6 M NaCl electrolyte.

Keywords Mg-air battery · Mg alloys · Electrochemical performance · Corrosion · Discharge

Introduction

Mg alloys are not only suitable as light structural materials in vehicles and aircraft but are also promising anode materials for Mg batteries because of their high catalytic activity [1, 2]. An Mg-air battery is an ideal power source due to its high theoretical voltage (3.09 V), energy density (3910 Wh kg^{-1}), low cost, and environmental friendliness [3, 4]. However, the Mg-air batteries are not as well utilized as the Zn-air batteries because of the less attractive performance of the Mg anode. One major problem is that corrosion products form and adhere to the Mg anode surface, causing anode polarization,

discharge potential decrease or even discharge stop [5–8]. In order to overcome these problems, it is necessary to control the composition of the Mg anode by choosing suitable alloying elements. For example, the addition of Li and Ce in Mg alloys improves anodic discharge [9]. The Mg–Al–Mn–Ca alloy exhibits superior discharge properties because Ca addition leads to the formation of thin passive discharge products on the anode surface and causes dissolution of the Mg matrix around Al_2Ca particles during discharge [10].

Another problem is hydrogen evolution-induced corrosion of the Mg anode during discharge, which reduces anode utilization factor. To overcome this effect, elements that result in a high hydrogen evolution initiation voltage can be added to Mg alloys [11–17]. Examples include Mg–Al–Zn [18], Mg–Hg–Ga [19], Mg–Li [20], and Mg–Al–Pb [21, 22]. Mg–Al–Pb alloys exhibit good discharge performance [23], but the lead is released from the alloy during the discharge process, which is detrimental to the environment.

Al is the most important alloying element for Mg, since the addition of Al results in better castability as well as increased compressive and fatigue strength. Commercial AZ alloys contain less than 10 wt% Al (maximum solubility is 12.7 wt% at the eutectic temperature of 437 °C), and Zn and Mn are used as secondary alloying elements. AZ series Mg alloys are widely used in industrial applications and contain Al and Zn, which improve the hydrogen evolution initiation

✉ Guangxin Wang
majingling@haust.edu.cn

✉ Alex A. Volinsky
volinsky@usf.edu

[1] Research Center for High Purity Materials, Henan University Science & Technology, Luoyang 471003, People's Republic of China

[2] Collaborative Innovation Center of Nonferrous Metals, Henan University of Science and Technology, Luoyang 471003, Henan Province, People's Republic of China

[3] Department of Mechanical Engineering, University of South Florida, 4202 E. Fowler Ave. ENB118, Tampa, FL 33620, USA

voltage of Mg [24, 25]. It is known that the corrosion of Mg–Al alloys greatly depends on the Al content.

To avoid the expense of Mg alloys, common 3N5 pure Mg (99.95 wt% purity with metallic impurities less than 0.05 wt%) and commercial Mg alloys AZ31, AZ61, and AZ91 were selected as anode materials for the Mg-air battery anodes in this paper. Our aim is to select a common commercial Mg alloy that can decrease passivation and hydrogen evolution-induced corrosion of the Mg anode for the Mg-air batteries.

Experiments

Materials and solution preparation

The as-cast 3N5 pure Mg and AZ31, AZ61, and AZ91 Mg alloys (provided by the Yueyang Aerospace New Material Co., LTD) were selected as anode materials. Their composition is listed in Table 1. The 0.6 M NaCl solution used as battery electrolyte was made from 99% pure NaCl (produced by the Sigma Aldrich) and distilled water.

For the electrochemical tests, samples with $\Phi 11.29 \times 5$ mm^2 dimensions were machined from pure Mg and Mg alloy ingots, ground with silicon carbide paper up to 1500 grit, rinsed with distilled water and ethyl alcohol, and air-dried.

Electrochemistry

Electrochemical measurements were performed with the three-electrode Model 600E Series Electrochemical Analyzer (CH Instruments, USA). The working electrodes were 3N5 pure Mg and Mg alloy samples, and the test solution was 0.6 M NaCl. The reference electrode was a saturated calomel electrode (SCE), and the counter electrode was a platinum plate. Samples were mounted in epoxy resin with an exposed 1 cm^2 surface area used as the working electrode. Electrochemical impedance spectroscopy (EIS) measurements were conducted with a 5-mV sine amplitude after the sample was exposed to the solution for 33 min. The test frequency was ranged from 0.1 to 100 kHz. After EIS measurements, potentiodynamic polarization tests were carried out at a scan rate of 1 mV s^{-1} from − 2 to − 1 V.

Table 1 Chemical composition of the 3N5 Mg and Mg alloys in wt%

Magnesium alloys	Al	Zn	Mn	Si	Mg
3N5	–	–	0.02	0.01	Balance
AZ31	3.16	0.83	0.31	0.03	Balance
AZ61	6.07	0.97	0.24	0.02	Balance
AZ91	8.92	0.94	0.28	0.04	Balance

Battery tests

An Mg-air battery consists of an anode, an air cathode, and an electrolyte. In this study, anodes are made of 3N5 Mg, AZ31, AZ61, and AZ91 alloys. The air cathode consists of a waterproof layer, a MnO$_2$ catalyst layer, and an electro-conductive skeleton (nickel mesh). A 0.6 M NaCl solution was used as the electrolyte. The discharge performance of the Mg-air battery was tested at a constant current of 20 mA cm^{-2} for 5 h using the LAND-CT2001A test system (Wuhan, China). Scanning electron microscopy (SEM, JSM-5610LV) and X-ray diffraction (XRD, D8 ADVANCE) were used for sample surface examination and to determine the corrosion products after discharge and before anode cleaning. SEM was used again to observe the anode surface after 5 min exposure to a cleaning solution containing 200 g l^{-1} CrO$_3$ and 10 g l^{-1} AgNO$_3$. Anode weight before and after discharge was measured by an electronic balance (AL204) with 10^{-4} g accuracy. The discharge capacity and the anode utilization factor were calculated using the following formulas:

$$\text{Discharge capacity} = \frac{i \times A \times t}{W_i - W_f} \quad (1)$$

$$\text{Anode utilization factor} = \frac{(i \times A \times t) \times M_a}{2F(W_i - W_f)} \times 100\% \quad (2)$$

Here, i is the current density (A cm^{-2}), t is the discharge time (sec), F is the Faraday constant (96,485 C mol^{-1}), A is the surface area (cm^2), M_a is the atomic mass (g mol^{-1}) of the sample, while W_i and W_f are weights of the sample before and after discharge (g), respectively.
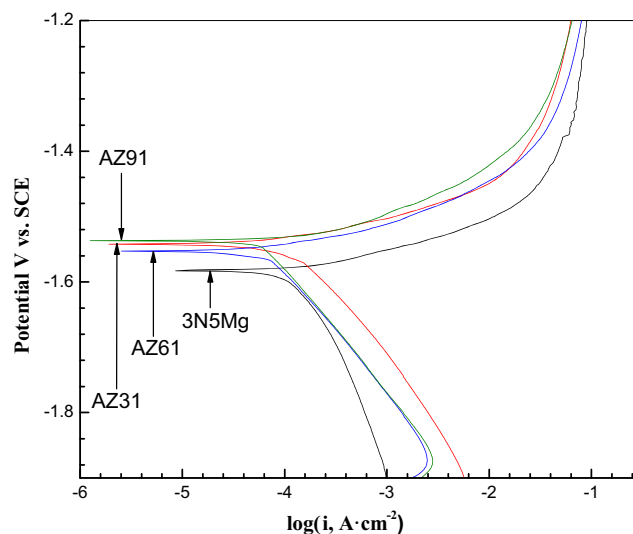

Fig. 1 Polarization curves of 3N5 Mg, AZ31, AZ61, and AZ91 alloys in 0.6 M NaCl solution

Table 2 Corrosion parameters of Mg alloys in the 0.6 M NaCl electrolyte

Magnesium alloys	E_{corr}, V vs. SCE	j_{corr}, mA cm^{-2}	R_p, Ω cm^2
3N5Mg	−1.583	0.44	61
AZ31	−1.542	0.19	120
AZ61	−1.553	0.16	139
AZ91	−1.537	0.30	82

Results and discussion

Polarization behavior

Figure 1 presents the polarization curves of 3N5 pure Mg and AZ31, AZ61, and AZ91 alloys in 0.6 M NaCl electrolyte. Table 2 lists the parameters calculated by the Tafel linear extrapolation. In Fig.1, the current density of 3N5 Mg is higher in the anodic potential region and lower in the cathodic potential region than other Mg alloys. AZ31, AZ61, and AZ91 alloys show a decline in current density and a positive shift of the potential, indicating that AZ series alloys have lower activation at corrosion potential (no discharge current). In Table 2, the AZ61 alloy has the lowest corrosion current density (j_{corr}, extrapolated from the potentiodynamic polarization curve) and the highest polarization resistance (R_p) of the alloys. The corrosion potential (E_{corr}) of the AZ61 alloy is
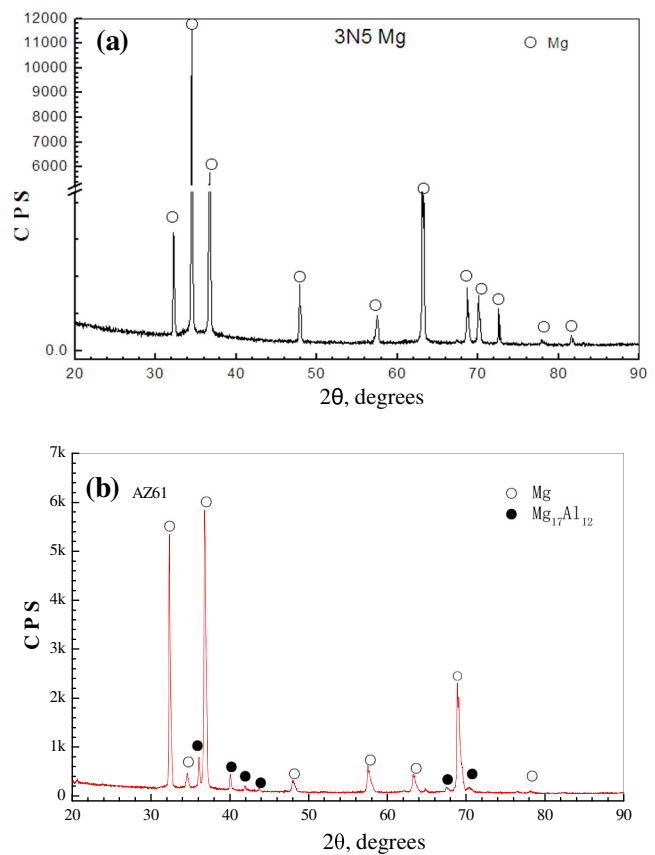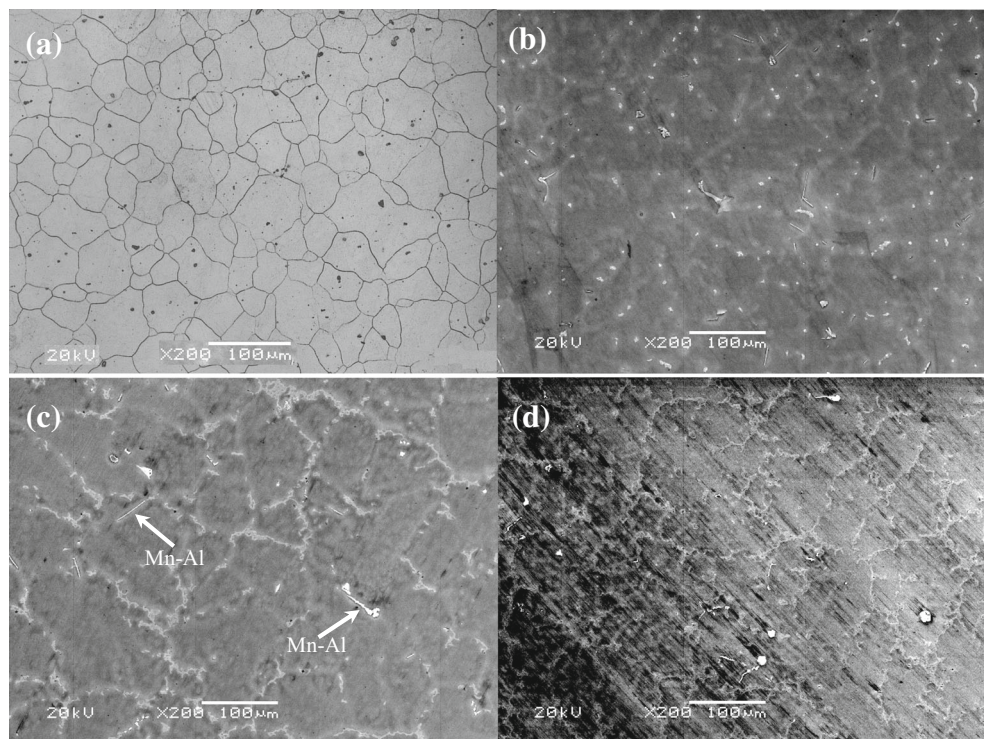
Fig. 3 XRD patterns of **a** 3N5 Mg and **b** AZ61 alloys

Fig. 2 Microstructure of **a** 3N5 Mg, **b** AZ31, **c** AZ61, and **d** AZ91 alloys
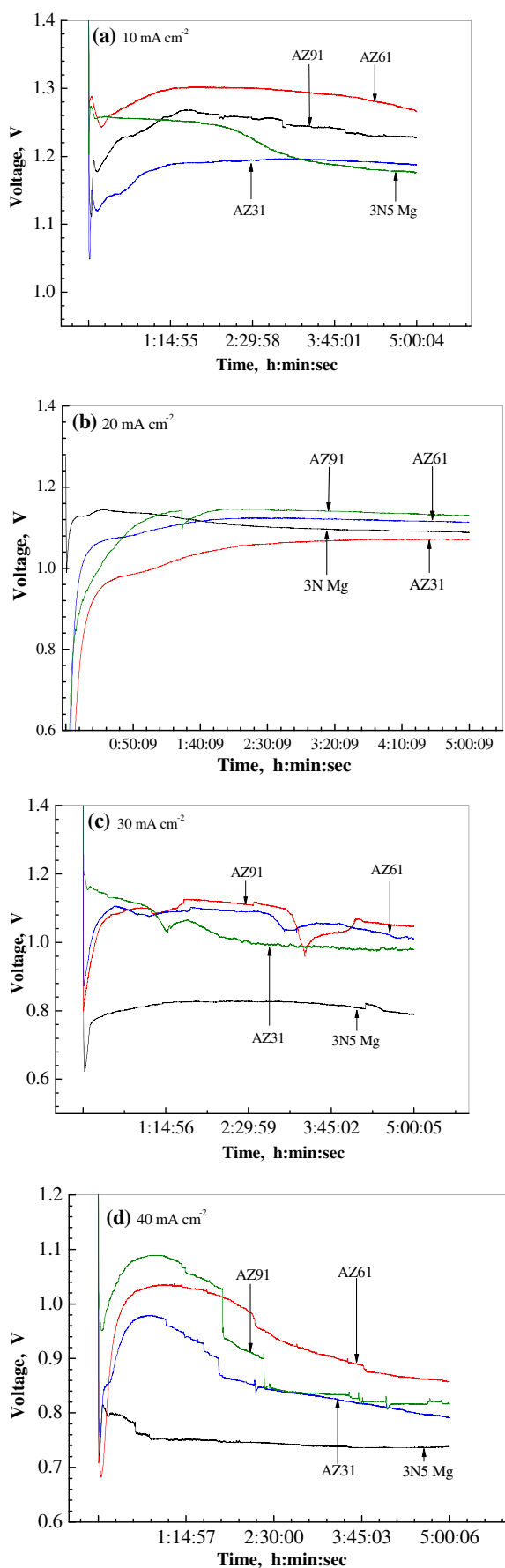
Fig. 4 Discharge curves of Mg–air batteries for 3N5 Mg, AZ31, AZ61, and AZ91 in 0.6 M NaCl solution: **a** 10 mA cm^{-2}, **b** 20 mA cm^{-2}, **c** 30 mA cm^{-2}, and **d** 40 mA cm^{-2}

higher than 3N5 Mg but lower than the AZ31 and AZ91 alloys. The electrochemical performance of the 3N5 Mg is lower than the 4N Mg [22], which may be related to the purity of magnesium and the test environment.

Surface morphology analysis

Figure 2 shows the SEM morphology of the 3N5 Mg and AZ31, AZ61, and AZ91 alloys. Figure 2a shows equiaxed grains of the 3N5 Mg. Figure 3 presents XRD patterns of the 3N5 Mg and the AZ61 alloy. Figures 2a and 3a indicate that only the α-Mg matrix exists in the 3N5 Mg alloy. The microstructure of the AZ31, AZ61, and AZ91 alloys is comprised of the α-Mg matrix and bright secondary phase particles with intermittent distribution along the grain boundaries, as seen in Fig. 2b–d. The amount of bright secondary phase particles is the highest in AZ91, followed by AZ61 and AZ31. The secondary phase particles of the AZ61 alloy are $Mg_{17}Al_{12}$, as illustrated in Fig. 3b; however, Mn-Al inclusions are too infrequent to be found. In Fig. 2b–d, AZ series alloys are seen to contain narrow strips or clumps of Mn-Al inclusions [26].

Table 3 The discharge performance of Mg-air cells (discharge current of 10 mA cm^{-2}, 20 mA cm^{-2}, 30 mA cm^{-2}, 40 mA cm^{-2}) for the 3N5 Mg, AZ31, AZ61, and AZ91 alloys in the 0.6 M NaCl solution

Materials	Current density, mA cm^{-2}	Operating voltage, V	Anode utilization factor, %
3N5Mg	10	1.226	30
AZ31	10	1.195	32
AZ61	10	1.3	41
AZ91	10	1.253	36
3N5Mg	20	1.102	34
AZ31	20	1.066	37
AZ61	20	1.128	45
AZ91	20	1.143	41
3N5Mg	30	0.827	39
AZ31	30	1.052	42
AZ61	30	1.09	47
AZ91	30	1.11	43
3N5Mg	40	0.748	41
AZ31	40	0.842	45
AZ61	40	0.94	52
AZ91	40	0.845	46

Battery performance

Figure 4 shows the discharge behavior of the Mg-air cells based on the 3N5 Mg, AZ31, AZ61, and AZ91 alloys measured at 10 mA cm^{-2}, 20 mA cm^{-2}, 30 mA cm^{-2}, and 40 mA cm^{-2} current density for 5 h. Table 3 summarizes the properties of these batteries. It can be seen that the anode utilization factor increases, but the operating voltage decreases with the current density increasing from 10 to 40 mA cm^{-2} for the Mg-air cells. This phenomenon is probably attributed to the suppression of the self-discharge reaction. Magnesium anodes in the NaCl solution can generate hydrogen by the following side reaction (3):

$$Mg + 2H_2O \rightarrow Mg(OH)_2 + H_2\uparrow \tag{3}$$
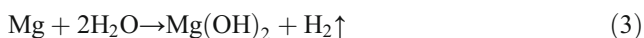
The main anodic reaction is:

$$2Mg + O_2 + 2H_2O \rightarrow 2Mg(OH)_2\downarrow \tag{4}$$

Thus, the self-discharge occurs along with the dissolution of the magnesium anode, and its mass loss is higher than what the Faraday law predicts. When the applied current density is increased, the anode utilization factor is obviously increased. There is a competition between the parasitic reaction (3), which consumes electrons to generate hydrogen and the main anodic reaction (4), which releases electrons to the external circuit. When discharged at a higher current density, more electrons flow to the external circuit because the magnesium oxidation rate increases dramatically, while the hydrogen generation rate increases only slightly. Therefore, the anodes exhibit higher anode utilization factor at higher current density. It can be seen from Fig. 4 and Table 3 that the operating voltage decreases with the discharge current density increasing from 10 to 40 mA cm^{-2} for the cells. This is mainly caused by the ohmic polarization. Higher current density results in more serious polarization and lower working potential. The Mg-air batteries with the AZ61 and AZ91 alloys have higher discharge potential than the 3N5 Mg and AZ31 alloys at the same current density. In the case of the AZ61 anode, the anode utilization factor can reach as high as 52% at 40 mA cm^{-2} current density for 5 h. The AZ61 alloy has better discharge properties in terms of the discharge voltage and the anode utilization factor, in spite of the discharge voltage of the AZ61 alloy being lower than the AZ91 alloy at 20 mA cm^{-2}.

Discharge morphology

Corroded morphology of the 3N5 Mg, AZ31, AZ61, and AZ91 alloys after discharge is displayed in Fig. 5. Discharge

Fig. 5 SEM micrographs of **a** 3N5 Mg, **b** AZ31, **c** AZ61, and **d** AZ91 after discharge in 0.6 M NaCl solution
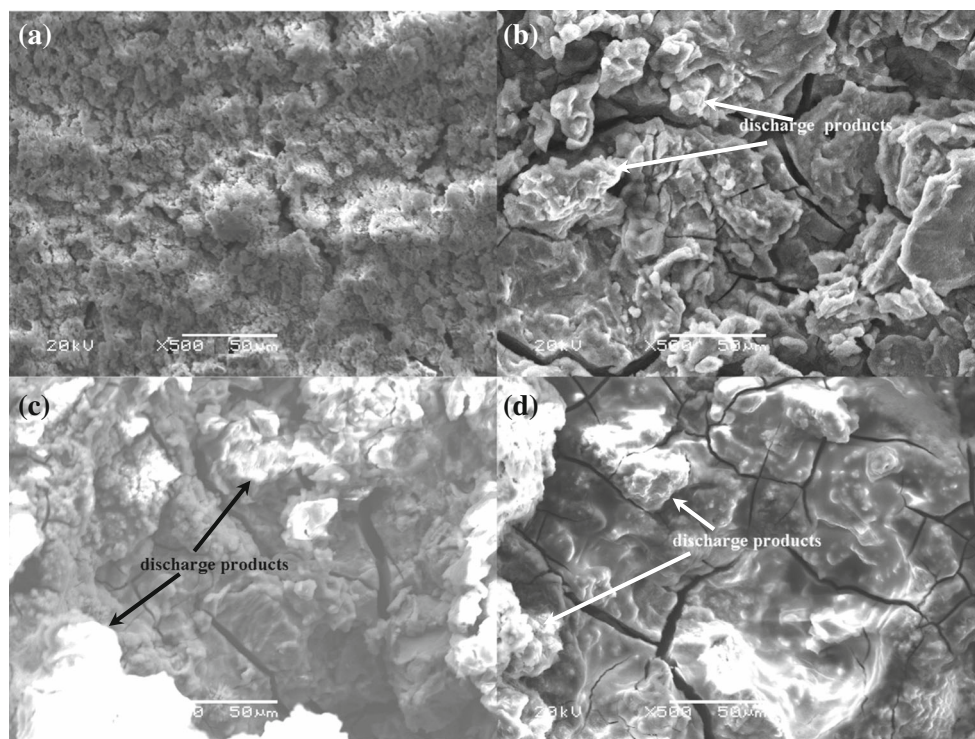
products are not obvious on the surface of the 3N5 Mg sample in Fig. 5a. However, small pieces of discharge products are observed on the surface of the AZ31 sample in Fig. 5b and bulk discharge products are formed on the surface of the AZ61 sample in Fig. 5c. The discharge products of AZ91 are smaller than AZ61. According to Fig. 2, the amount of secondary phases is the highest in AZ91, followed by AZ61, AZ31, and 3N5 Mg alloys. The precipitated phases need to be considered during the discharge process of the samples because they are directly related to the dissolution process of the alloys. The secondary phases not only accelerate dissolution of the Mg matrix around the secondary $Mg_{17}Al_{12}$ phase particles during discharge but also result in more corrosion products. The accumulation of discharge products somewhat prohibits hydrogen-induced corrosion of the AZ61 and AZ91 samples, so the two samples present higher anodic efficiency than the 3N5 Mg and AZ31 samples. Discharge products accumulate more easily on the surface of the AZ61 alloy in Fig. 5c. Thus, the AZ61 anode exhibits the lowest corrosion current density (j_{corr}) and the highest anode utilization of the alloys.

XRD patterns of the 3N5 Mg and AZ91 alloys after discharge in 0.6 M NaCl solution and before cleaning are presented in Fig. 6. Figure 6a shows that the corrosion products of the 3N5 Mg mainly contain $Mg(OH)_2$, $Mg_2(OH)ClCO_3$, and Mg. Figure 6b illustrates that the corrosion products of the AZ91 alloy mainly contain $Mg(OH)_2$, $Mg_{17}Al_{12}$, $Mg_2(OH)ClCO_3$, and Mg. $Mg(OH)_2$ results from the desirable Mg-air battery reaction (4) and the hydrogen evolution corrosion reaction (3), which occurs on the Mg anode.

Furthermore, $Mg_{17}Al_{12}$ precipitates act as galvanic cathodes, promoting hydrogen evolution-induced corrosion of the Mg matrix [27, 28]. As the Mg matrix around $Mg_{17}Al_{12}$ precipitates corrodes away, the $Mg_{17}Al_{12}$ precipitates break off. For the AZ91alloy, the amount of the $Mg_{17}Al_{12}$ precipitates is higher, and they break off easier. Moreover, $Mg_{17}Al_{12}$ corrosion products can damage the stability of $Mg(OH)_2$ and $Mg_2(OH)ClCO_3$ films through the corrosion product combination process [29]. Therefore, it is difficult to form an accumulated layer of corrosion products on the AZ91 alloy surface during the discharge process. Thus, the AZ91 alloy can have a higher operating voltage compared to the other alloys.

The amount of discharge products of AZ31 is smaller than AZ61 in Fig. 5, but the voltage of AZ61 is higher than AZ31 in Fig. 4. For Mg alloys, the stability of the discharge products can be improved when the Al element dissolves in the α-Mg matrix [3]. Increasing the Al concentration in the α-Mg matrix increases anode
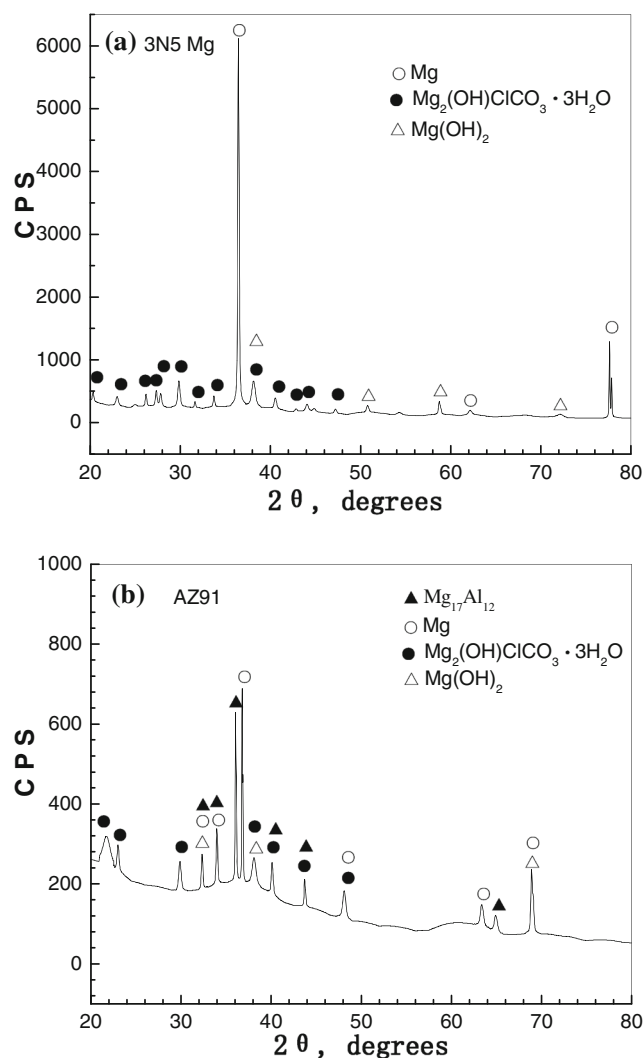

Fig. 6 XRD patterns of a 3N5 Mg and b AZ91 alloys after discharge in 0.6 M NaCl solution

dissolution rate [30]. This is due to the growth of the Al-enriched surface layer. The Al concentration in the discharge products increased with Al content in the α-Mg matrix and the Al^+ ions control the mass transport of water and other ions through the interlayers [30]. This benefits the dissolution of the α-Mg matrix.

Corroded morphology of the samples after discharge products removal is shown in Fig. 7. The image in Fig. 7a indicates that 3N5 Mg undergoes a severe and nonuniform corrosion attack. This phenomenon is partially due to the higher hydrogen evolution-induced corrosion of pure Mg during discharge. According to Fig. 7b, the AZ31 alloy suffers a uniform attack across the entire alloy surface. This is explained by the activation of randomly distributed $Mg_{17}Al_{12}$ particles in Fig. 2b, which possibly act as an efficient cathode for promoting corrosion of the Mg matrix. On the other hand, the AZ61 alloy undergoes less corrosion damage with large areas being unaffected. Therefore, the protective effect of the $Mg_{17}Al_{12}$ phase

[26], which can act as a barrier to prevent the self-peeling of discharge products, makes it difficult for the discharge products to fall away from the AZ61 sample surface. The net-like $Mg_{17}Al_{12}$ phase in Fig. 2c forms a strong galvanic coupling with the α-Mg matrix. According to Fig. 7d, the AZ91 sample corroded more compared to the AZ61 sample, suggesting that the protective effect of the secondary phases is decreased. This is due to the break off of the $Mg_{17}Al_{12}$ precipitates and corrosion products formation, which damage the stability of the $Mg(OH)_2$ and $Mg_2(OH)ClCO_3$ films.

Electrochemical impedance spectroscopy

Figure 8 presents the Nyquist plots of the 3N5 Mg and AZ31, AZ61, and AZ91 alloys in 0.6 M NaCl solution. Three tests were conducted, and the shape of the electrochemical impedance spectroscopy (EIS) plots is similar for all samples, indicating similar corrosion behavior of 3N5 Mg and AZ series alloys in the 0.6 M NaCl solution. All diagrams include a high-frequency capacitive loop as well as a low-frequency inductive loop. In general, a capacitive semicircle at high frequency is attributed to double-layer capacitance and charge transfer resistance [31]. Several authors have related this arc to metal dissolution during the corrosion process, with its diameter being associated with charge transfer resistance, and subsequently, with corrosion resistance [32, 33]. According to this, the AZ91 and AZ61 alloys exhibited greater corrosion resistance than the AZ31 alloy and 3N5 Mg.

EIS results are described by an equivalent circuit in Fig. 8c, showing R_s, R_t, CPE_1, L, and R_1 elements. For better fitting results, the capacitance element (C) representing double-layer capacitance is replaced with a constant phase element (CPE) [34, 35]. The impedance of CPE is defined as [36]:

$$Z_{CPE} = Q^{-1}(j\omega)^{-n} \tag{5}$$

where Q is the CPE constant, j is an imaginary unit, n is the CPE power ($-1 \leq n \leq 1$), and ω is the angular frequency ($\omega = 2\pi f$, where f is the frequency). Obviously, CPE is a pure capacitance when n is 1. n values close to 0.5 are indicative of diffusion, and consequently, CPE represents the Warburg diffusion component. Furthermore, CPE represents a resistance for n values close to 0, and an inductance for n close to -1. R_s represents the solution resistance; R_t and CPE_1 are the charge transfer resistance and double-layer capacitance, respectively. L and R_1 represent the corresponding parameters for mass transport in the surface corrosion products layer. Based on the equivalent circuits in Fig. 8c, electrochemical parameters can be derived from EIS. Table 4 shows the electrochemical parameters obtained according to the equivalent circuit in Fig. 8c by using the ZSimpwin software. It shows that R_t increases in the following order: 3N5 Mg < AZ31 < AZ61 < AZ91. This means that hydrogen evolution-induced corrosion decreases in the following order: 3N5 Mg > AZ31 > AZ61 > AZ91.

Fig. 7 SEM micrographs of **a** 3N5 Mg, **b** AZ31, **c** AZ61, and **d** AZ91 alloys after discharge at 20 mA cm^{-2} for 5 h in the 0.6 M NaCl solution
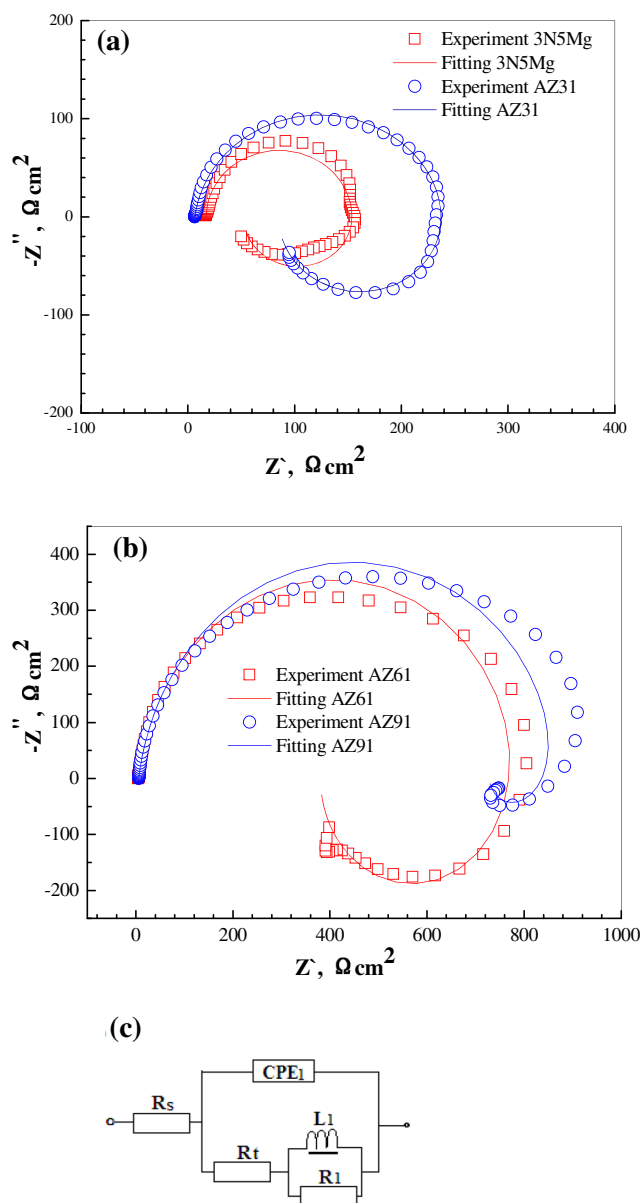
(a)

(b)

(c)
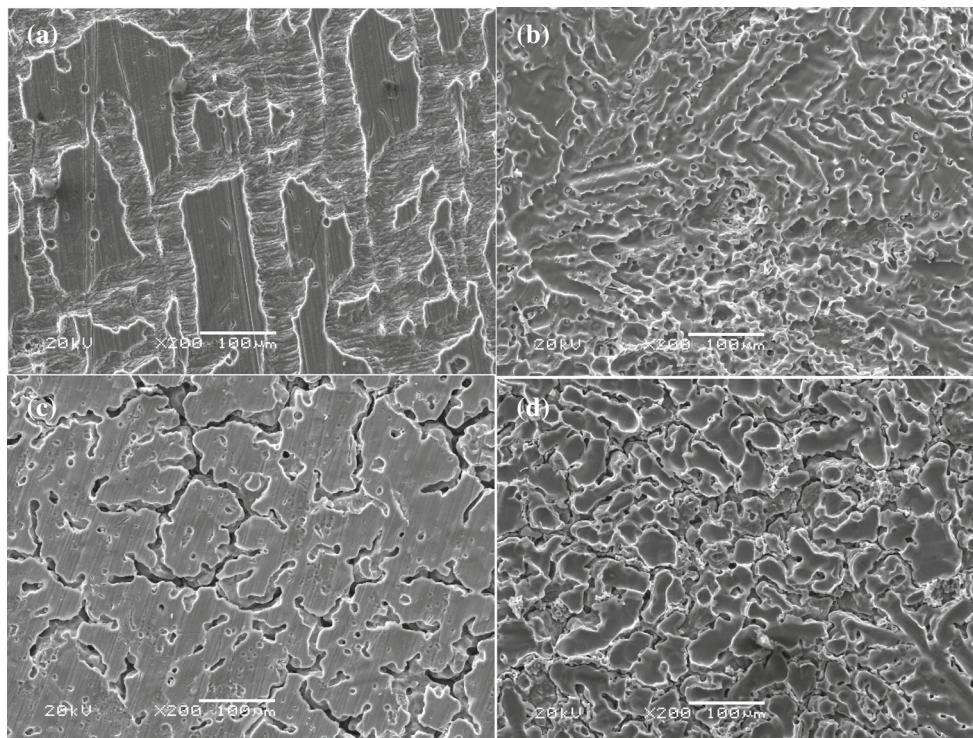
Fig. 8 EIS spectra of **a** 3N5 Mg and AZ31, **b** AZ61 and AZ91 alloys in the 0.6 M NaCl solution, and **c** the EIS equivalent circuit $R_s(Q_1(R_t(L_1R_1)))$

It has been proposed [37, 38] that a low-frequency inductive loop is associated with the performance of the alloy surface discharge products layer. As seen in Table 4, the R_1 value of the AZ91 sample is smaller than the AZ31 and AZ61. R_1 represents the mass transport resistance in the surface corrosion products layer. There are fewer discharge products on the surface of the AZ91 sample, so it is possible that anode utilization is reduced.

Conclusions

The purpose of this study was to select a common commercial Mg alloy to function as anode in Mg-air batteries with a 0.6 M NaCl electrolyte, with low anode passivation and reduced hydrogen evolution-induced corrosion. Corrosion and discharge performance of Mg-air batteries based on 3N5 Mg, AZ31, AZ61, and AZ91 alloys was studied. It was found that corrosion of Mg alloys in the 0.6 M NaCl solution was reduced by increasing the amount of alloyed Al. For 3N5 Mg, AZ31, and AZ61, increased Al content reduced corrosion susceptibly and gradually increased anode utilization factor. The key factors for improved performance of the AZ61 alloy were associated with the $Mg_{17}Al_{12}$ phase, which can act as a barrier to prevent the self-peeling of discharge products. For the AZ91 alloy, the addition of 8–9 wt% Al drastically decreased corrosion resistance and increased the discharge activation. This is due to the break off of $Mg_{17}Al_{12}$ precipitates and the formation of corrosion products, which damage the stability of the $Mg(OH)_2$ film and decrease the accumulation of corrosion products on the AZ91 alloy surface. EIS and SEM characterization supports the results of electrochemical and discharge performance tests. It is concluded that the AZ61 alloy is the best-suited material to serve as the anode for the Mg-air battery in 0.6 M NaCl electrolyte.

Table 4 EIS simulated values of the 3N5 Mg and Mg alloys in the 0.6 M NaCl solution

Magnesium alloys	3N5Mg	AZ31	AZ61	AZ91
R_s, Ω cm^2	17.32	6.62	5.28	5.9
$CPE_1 \times 10^{-6}$, F cm^{-2}	9.19	19.95	12.56	12.29
n_1 (0 < n < 1)	1	0.92	0.92	0.91
R_t, Ω cm^2	34.81	78.47	375.3	724.4
$L_1 \times 10^{-7}$, H cm^2	28.26	36.8	48.21	21.87
R_1, Ω cm^2	101.7	156.1	430.3	161.2
x^2	5.17×10^{-3}	2.76×10^{-3}	5.02×10^{-3}	2.89×10^{-3}

References

1. Cheng F, Chen J (2012) Metal–air batteries: from oxygen reduction electrochemistry to cathode catalysts. Chem Soc Rev 41:2172–2192

2. Xiong HQ, Zhu HL, Luo J, Yu K, Shi CL, Fang HJ, Zhang Y (2017) Effects of heat treatment on the discharge behavior of Mg-6wt.%Al-1wt.%Sn alloy as anode for magnesium-air batteries. J Mater Eng Perf 26:2901–2911

3. Zheng TX, Hu YB, Zhang YX (2018) Composition optimization and electrochemical properties of Mg-Al-Sn-Mn alloy anode for Mg-air batteries. Mater Des 137:245–255

4. Xiong HQ, Yu K, Yin X (2017) Effects of microstructure on the electrochemical discharge behavior of Mg-6wt%Al-1wt%Sn alloy as anode for Mg-air primary battery. J Alloys Compd 708:652–661

5. Yuasa M, Huang XS, Suzuki KK, Mabuchi M, Chino Y (2014) Effects of Microstructure on Discharge Behavior of AZ91 Alloy as Anode for Mg–Air Battery. Mater Trans 55:1202–1207

6. Yan YJ, Daniel G, Cristina PG (2017) Investigating discharge performance and Mg interphase properties of an Ionic Liquid electrolyte based Mg-air battery. Electrochim Acta 235:270–279

7. Li XD, Lu HM, Yuan SQ (2017) Performance of Mg–9Al–1In alloy as anodes for Mg-air batteries in 3.5 wt% NaCl solutions. J Electrochem Soc 164:A3131–A3137

8. Law YT, Schnaidt J, Brimaud S (2016) Oxygen reduction and evolution in an ionic liquid ([BMP][TFSA]) based electrolyte: a model study of the cathode reactions in Mg-air batteries. J Power Sources 333:173–183

9. Ma YB, Li N, Li DY, Zhang ML, Huang XM (2011) Performance of Mg–14Li–1Al–0.1Ce as anode for Mg-air battery. J Power Sources 196:2346–2350

10. Yuasa M, Huang X, Suzuki K, Mabuchi M, Chino Y (2015) Discharge properties of Mg–Al–Mn–Ca and Mg–Al–Mn alloys as anode materials for primary magnesium–air batteries. J Power Sources 297:449–456

11. Cao D, Wu L, Wang G, Lv Y (2008) Electrochemical oxidation behavior of Mg–Li–Al–Ce–Zn and Mg–Li–Al–Ce–Zn–Mn in sodium chloride solution. J Power Sources 183:799–804

12. Wang N, Wang R, Peng C, Feng Y (2014) Enhancement of the discharge performance of AP65 magnesium alloy anodes by hot extrusion. Corros Sci 81:85–95

13. Wang N, Wang R, Peng C, Feng Y, Chen B (2012) Effect of hot rolling and subsequent annealing on electrochemical discharge behavior of AP65 magnesium alloy as anode for seawater activated battery. Corros Sci 64:17–27

14. Feng Y, Wang R, Peng C, Qiu K, Wang N, Zhang C, Zhang J (2010) Corros Sci 52:3474–3480

15. Feng Y, Wang R, Peng C (2013) Influence of Ga and In on microstructure and electrochemical properties of Mg anodes. Nonferrous Met Soc China 23:2650–2656

16. Wang N, Wang R, Peng C, Feng Y (2012) Effect of manganese on discharge and corrosion performance of magnesium alloy AP65 as anode for seawater-activated battery. Corrosion 68:388–397

17. Lv Y, Liu M, Xu Y, Cao D, Feng J (2013) The electrochemical behaviors of Mg–8Li–3Al–0.5Zn and Mg–8Li–3Al–1.0Zn in sodium chloride solution. J Power Sources 225:124–128

18. Huang G, Zhao Y, Wang Y, Zhang H, Pan F (2013) Performance of Mg–air battery based on AZ31 alloy sheet with twins. Mater Lett 113:46–49

19. Zhao J, Yu K, Hu Y, Li S, Tan X, Chen F, Yu Z (2011) Electrochim. Acta 56:8224–8231

20. Lv Y, Xu Y, Cao D (2011) The electrochemical behaviors of Mg, Mg–Li–Al–Ce and Mg–Li–Al–Ce–Y in sodium chloride solution. J Power Sources 196:8809–8814

21. Yu K, Huang Q, Zhao J, Dai Y (2012) Electrochemical properties of magnesium alloy anodes discharged in seawater. T Nonferr Metal Soc 22:2184–2190

22. N.G. Wang, Y.C. Mu, Q. Li, Z.C. Shi. RSC Adv, 7 (2017) 53226–53235, Discharge and corrosion behaviour of AP65 magnesium anode plates with different rolling reductions

23. Wang N, Wang R, Peng C, Peng B, Feng Y, Hu C (2014) Discharge behaviour of Mg-Al-Pb and Mg-Al-Pb-In alloys as anodes for Mg-air battery. Electrochim. Acta 149:193–205

24. Umoren SA, Li Y, Wang FH (2011) Effect of aluminium microstructure on corrosion and inhibiting effect of polyacrylic acid in H2SO4 solution. J Appl Electrochem 41:307–315

25. Zhao C, Huang GS, Zhang C (2018) Rare Metal Mater Eng 7: 1064–1068

26. Pardo A, Merino MC, Coy AE, Viejo F, Arrabal R, Feliú S (2008) Influence of microstructure and composition on the corrosion behaviour of Mg/Al alloys in chloride media. Electrochim Acta 53: 7890–7902

27. Song G (2009) Effect of tin modification on corrosion of AM70 magnesium alloy. Corros Sci 51:2063–2070

28. Song G, Bowles AL, StJohn DH (2004) Corrosion resistance of aged die cast magnesium alloy AZ91D. Mater Sci Eng A 366:74–86

29. Yuan S, Lu H, Sun Z, Fan L, Zhu X, Zhang W (2016) Electrochemical performance of Mg-3Al modified with Ga, In and Sn as anodes for Mg-air battery. J Electrochem Soc 163: A1181–A1187

30. G.L. Song, A. Atrens, X.N. Wu, B. Zhang. Corros Sci, 40 (1998) 1769–1791, Corrosion behaviour of AZ21, AZ501 and AZ91 in sodium chloride

31. Moutarlier V, Gigandet MP, Normand B, Pagetti J (2005) EIS characterisation of anodic films formed on 2024 aluminium alloy, in sulphuric acid containing molybdate or permanganate species. Corros Sci 47:937–945

32. Chen X, Tian WM, Li SM, Yu M, Liu JH (2016) Chin J Aeronautics 29:114–120

33. Dornbusch DA, Hilton R, Gordon MJ, Suppes GJ (2013) ECS Electrochem. Lett 2(9):A89–A95

34. Bethencourt M, Botana FJ, Cano MJ, Marcos M, Sánchez-Amaya JM, González-Rovira L (2008) Using EIS to analyse samples of Al–Mg alloy AA5083 treated by thermal activation in cerium salt baths. Corr Sci 50:1376–1384

35. Rosalbino F, Angelini E, Macciò D, Saccone A, Delfino S (2009) Application of EIS to assess the effect of rare earths small addition on the corrosion behaviour of Zn–5% Al (Galfan) alloy in neutral aerated sodium chloride solution. Electrochim Acta 54:1204–1209

36. Osório WR, Peixoto LC, Garcia A (2013) The effects of Ag content and dendrite spacing on the electrochemical behavior of Pb–Ag alloys for Pb-acid battery components. J Power Sources 238:324–335

37. Lv YZ, Bao LL, Meng F (2018) The electrochemical behaviors of Mg-5Li-3Al-1La and Mg-8Li-3Al-1La alloys in sodium chloride solution. Ionics 24:1715–1720

38. Zhao YC, Huang GS, Zhang C (2018) Rare Metal Mater Eng 47: 1064–1068